

# Back to the Color: Learning Depth to Specific Color Transformation for Unsupervised Depth Estimation

Yufan Zhu, Chongzhi Ran, Mingtao Feng, Weisheng Dong, *Member, IEEE*, Antonio M. López, *Member, IEEE*, and Guangming Shi, *Fellow, IEEE*

**Abstract**—Virtual engines have the capability to generate dense depth maps for various synthetic scenes, making them invaluable for training depth estimation models. However, synthetic colors often exhibit significant discrepancies compared to real-world colors, thereby posing challenges for depth estimation in real-world scenes, particularly in complex and uncertain environments encountered in unsupervised monocular depth estimation tasks. To address this issue, we propose Back2Color, a framework that predicts realistic colors from depth utilizing a model trained on real-world data, thus facilitating the transformation of synthetic colors into real-world counterparts. Additionally, by employing the Syn-Real CutMix method for joint training with both real-world unsupervised and synthetic supervised depth samples, we achieve improved performance in monocular depth estimation for real-world scenes. Moreover, to comprehensively address the impact of non-rigid motions on depth estimation, we propose an auto-learning uncertainty temporal-spatial fusion method (Auto-UTSF), which integrates the benefits of unsupervised learning in both temporal and spatial dimensions. Furthermore, we design a depth estimation network (VADEPTH) based on the Vision Attention Network. Our Back2Color framework demonstrates state-of-the-art performance, as evidenced by improvements in performance metrics and the production of fine-grained details in our predictions, particularly on challenging datasets such as Cityscapes for unsupervised depth estimation. Code is available at <https://github.com/BlueEg/back2color/>.

**Index Terms**—Back to the Color, auto-learning uncertainty, Vision Attention Depth Network

## I. INTRODUCTION

IN the real world, even after prolonged evolution, humans are still limited to qualitatively analyzing the depth of specific points in their field of view to assist in their actions [1]. Despite significant technological advances, the acquisition of precise and dense depth information remains a formidable challenge [2], [3]. Even with the refinement of advanced LiDAR systems [3], their data are inherently sparse, comprising only discrete depth points. Even the most precise scanning LiDAR systems can provide only sparse depth points. Unsupervised depth estimation, powered by epipolar geometry [4] using purely visual approaches does not require additional annotation for depth information other than camera parameters. Unsupervised depth estimation eliminates the need to create specific datasets for particular scenes [5]. By utilizing binocular and motion disparity clues, it mimics the structure of human vision, making it efficient and cost-effective [6].

This paper was produced by the IEEE Publication Technology Group. They are in Piscataway, NJ.

Manuscript received April 19, 2021; revised August 16, 2021.

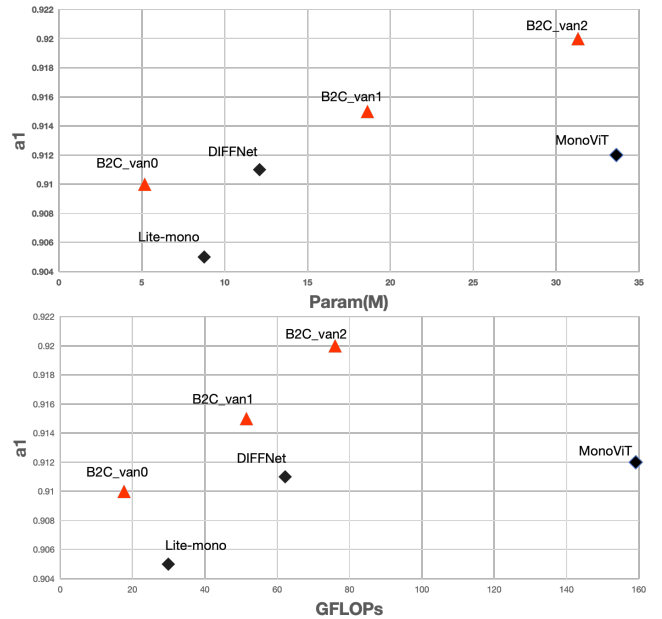


Fig. 1. Performance vs. model efficiency on KITTI at a resolution of  $320 \times 1024$ . Our Back2Color method has advantages in both accuracy and speed.

This is why many researchers and companies are actively pursuing this approach [7]. Monodepth2 [8], the most renowned framework for unsupervised monocular depth estimation, has established itself as a classic and successful method. By reprojecting related frames (temporal and spatial) and regressing depth values. This adaptability enables Monodepth2 to obtain depth information for various scenes through adaptive fine-tuning, making it highly versatile. However, despite its strengths, Monodepth2 has several limitations. Firstly, the auto-masking for handling non-rigid moving objects, follows a simple rule: the pixel error after reprojection should be less than before reprojection. This pixel-level determination cannot ensure effectiveness in smooth regions. Additionally, when applied to more complex datasets such as Cityscapes [9], it almost fails. Secondly, photometric reprojection error also fails in areas with no texture or with texture-less background objects, leading to depth prediction failure. Lastly, methods based on photometric reprojection matching lack prior knowledge of the objective structure. These issues make it challenging for unsupervised depth estimation methods to be applied in real world.

With the continuous advancement of computer graphics

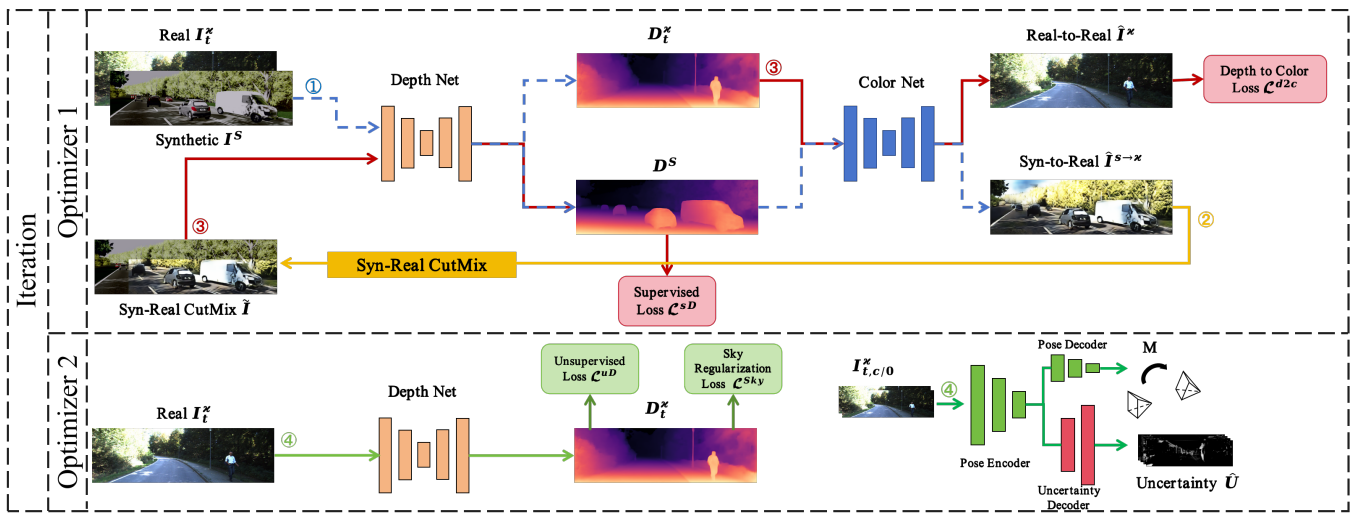


Fig. 2. **Illustration of our framework.** Using Optimizer 1, we train supervised Syn-Real depth estimation and the Color Net to predict real colors from depths. First, ①we fix the Depth Net and Color Net to infer real and synthetic predicted depths, using the synthetic depth to predict Syn-to-Real Color. Then, ②we apply Syn-Real Cutmix to create new syn-real colors, ③optimizing the Depth Net with synthetic groundtruth and the Color Net on real dataset. With Optimizer 2, ④we train real-world unsupervised depth estimation with sky regularization loss and auto-learning uncertainty. The dotted line indicates inference only.

and virtual engine technologies, significant progress has been made in the creation and application of virtual urban scene datasets [9]–[13]. The evolution of 3D virtual engines, such as Unity and Unreal Engine [14], [15], has played a crucial role in enhancing the realism and visualization effects of virtual urban scenes. These engines not only facilitate finer scene modeling but also provide interactivity and dynamism, making virtual urban scene data more closely resemble the real world. Synthetic datasets [10] can provide precise qualitative data for virtual urban scenes, including depth, semantic labels, and more. Therefore, it would be desirable if synthetic depth could be used to assist in the unsupervised depth estimation of real-world [16]. Compared to synthetic datasets, real-world depth estimation datasets [9], [17] have the following notable drawbacks: firstly, synthetic depth data is dense, whereas depth data collected by LiDAR is sparse and discrete [17]. Secondly, depth computed through stereo matching suffers from occlusions and lacks accuracy due to the short baseline [9]. Additionally, sparse depth sampling does not provide sufficient information for learning when obstacles are small or distant (resulting in small apparent areas), making it challenging for the network to accurately reconstruct their shapes.

In this paper, our Back2Color learns the mapping process in the target domain (Real). This mapping is then applied to the source domain (Synthetic) to reduce the gaps between colors of the source and target domains. Additionally, we introduced an improved version of CutMix [18], termed Syn-Real CutMix, to effectively combine real-world, synthesized, and syn-to-real data in both batch and image spatial dimensions. By incorporating Syn-Real CutMix into our training process, we were able to enrich the training dataset with more diverse color-to-depth knowledge extracted from synthetic scenes. Furthermore, the joint training with diverse data sources enables the model to capture a wider range of color and depth variations present in real-world scenes, thus

enhancing its robustness and generalization capability.

Additionally, we addressed the issue of chaotic depth clouds(5) by proposing a Background Textureless regularization loss (sky regularization loss), aiming to narrow the gap between predicted depths from real-world and synthesized data. Through joint training, our method enables the unsupervised monocular depth estimation to leverage knowledge from synthesized data, resulting in the generation of dense and sharp depths.

In pursuit of higher prediction accuracy and a more lightweight model compared to Transformer-based methods, we introduced the Vision Attention Network [19](VAN) as the backbone and equipped it with an efficient single-path high-resolution decoder, forming the new Vision Attention Depth Net(VADepth). Our design demonstrated more effective performance than Transformers. In our in-depth experiments, we found that Auto-masking is not always effective in identifying non-rigid moving objects with the same direction and speed. Additionally, it cannot handle vehicles moving in opposite directions, leading to significant errors in depth estimation. Therefore, we introduce the automatic learning uncertainty estimation fusion method [20], effectively combining the advantages of temporal-spatial unsupervised approaches, termed Auto-learning Uncertainty Temporal-Spatial Fusion(Auto-UTSF). This method thoroughly resolves the issue of non-rigid motion in unsupervised estimation, greatly improving the accuracy of depth estimation. To summarize, the key contributions of our work include:

- To address the issue of color and texture discrepancies between synthetic and real-world datasets, we propose Back2Color. This framework stores the color information of specific scenes (target domain) within the model, enabling the reverse prediction of color images from depth data. Additionally, we introduce Syn-Real CutMix to harmonize the joint training of real-world and synthetic

data, thereby enhancing the effectiveness of unsupervised depth estimation in real-world scenes.

- We designed an efficient and lightweight Depth Net based on the Vision Attention Network. This network features fewer parameters and lower computational complexity compared to transformer-based networks, while achieving superior performance.
- Furthermore, to more robustly recognize non-rigid moving objects and address occlusion issues in stereo systems, we enhance the method based on Auto-Uncertainty by introducing Auto-Spatial-Temporal Uncertainty Fusion, which leverages complementary spatial and temporal advantages in the unsupervised depth estimation process.
- Experimental results demonstrate that our method surpasses all transformer-based models, achieving state-of-the-art (SOTA) metrics while maintaining manageable computational costs. Additionally, the visual boundaries of the estimated depth images are clearer.

## II. RELATED WORKS

### A. Unsupervised Depth Estimation

Unsupervised depth estimation aims to predict distances from stereo views or video sequences. Initial methods like those by Godard et al. [21] introduced disparity consistency loss, while Zhou et al. [22] pioneered depth and pose estimation simultaneously. Recent advancements [23]–[27] refine network structures for higher accuracy. Techniques like PackNet [23] and CADepth [24] enhance geometric and appearance information propagation. HR-Depth [25] and DIFFNet [26] utilize HRNet for better resolution utilization. RA-Depth [27] employs HRNet for both encoding and decoding. In natural language processing, the Transformer architecture [28] has been successful, later adapted to computer vision tasks [29], [30]. It serves as the backbone for depth estimation [31]–[35], but faces challenges like computational demands and real-time constraints. Existing methods prioritize model architecture, often overlooking crucial obstacles and targets.

### B. Depth Estimation with Synthetic data

Researchers have already attempted to use synthesized dense depths to guide the training of real-world depth estimation [16], [36]. Gurram et al. [16] categorized this problem as a dimension adaptation problem, where the objective is to adapt models trained on a source(synthesized) domain to perform well in a different target domain(real-world). They employed the Gradient Reverse Layer [37] to identify features from different domains during back propagation. Swami et al. [36], on the other hand, simultaneously trained on both synthesized and real-world datasets, leveraging scale information in Synthetic dataset to recover scale in unsupervised depth estimation. To bridge the gap between real-world and synthetic datasets in the image domain, Zhao et al. [38] leveraged synthetically rendered data and employed image translation techniques to narrow the synthetic-real domain gap, thereby enhancing monocular depth prediction.

### C. Style transfer in urban scenes

Research on style transfer for urban scene images has long been ongoing due to its importance in autonomous driving technology. Isola et al. [39] proposed a conditional GAN framework for generating urban scene images from semantic segmentation images of Cityscapes in 2017. However, generative models may produce random and plausible objects, disrupting the scene structure, as shown in their experiments. Atapour et al. [40] utilized style transfer and adversarial training to convert real-world color images into synthetic environment-style images. Huang et al. [41] applied GAN-based domain transfer for data augmentation in urban scene weather-time conversion. To minimize the visual gap between source and target domains, Gomez et al. [42] aligned colors across different domains in the Lab color space. Zheng et al. [43] used GANs to convert synthetic colors to real-world colors.

## III. METHODOLOGY

In this section, we will first introduce our Back2Color method, which involves learning the depth-to-color mapping relationship in the target domain to train the Color Net. This method also includes the spatial-batch joint training technique named Real-Syn CutMix and an approach for handling background textureless objects. Next, We will introduce our Depth Net based on the Vision Attention Network, which balances performance and lightweight design. Finally, we will present a more robust method, Auto-learning Uncertainty Temporal-Spatial Fusion (Auto-UTSF), to recognize and solve non-rigid motion problems.

### A. Back to the Color

1) *Transform depth to specific colors*: the significant gap between synthetic and real-world color images arises from the inherent complexity of the real world. Colors in real-world scenes are influenced by various factors, including lighting intensity, surface material of obstacles, and smoothness. Each of these factors is intricate and highly variable, making them challenging to simulate realistically using typical 3D engines. As a result, discerning the origin of an image intuitively is feasible, both for humans and deep learning alike. Consequently, directly combining real-world and synthetic datasets for training essentially involves dealing with two distinct domains. Our Back2Color approach learns the mapping relationship in the target domain(Real). This mapping is then applied to the source domain (Synthetic) to reduce the gaps between colors of the source and target domains.

Predicting depth from color entails extrapolating 3D information from optical data, mirroring the process carried out by the human brain. Throughout training, neural networks assimilate various factors such as obstacle features, perspective and occlusion relationships, fine-grained surface details, apparent surface areas, as well as lighting and shadow effects [44]. It acquired features are subsequently leveraged to estimate the depth of obstacles.

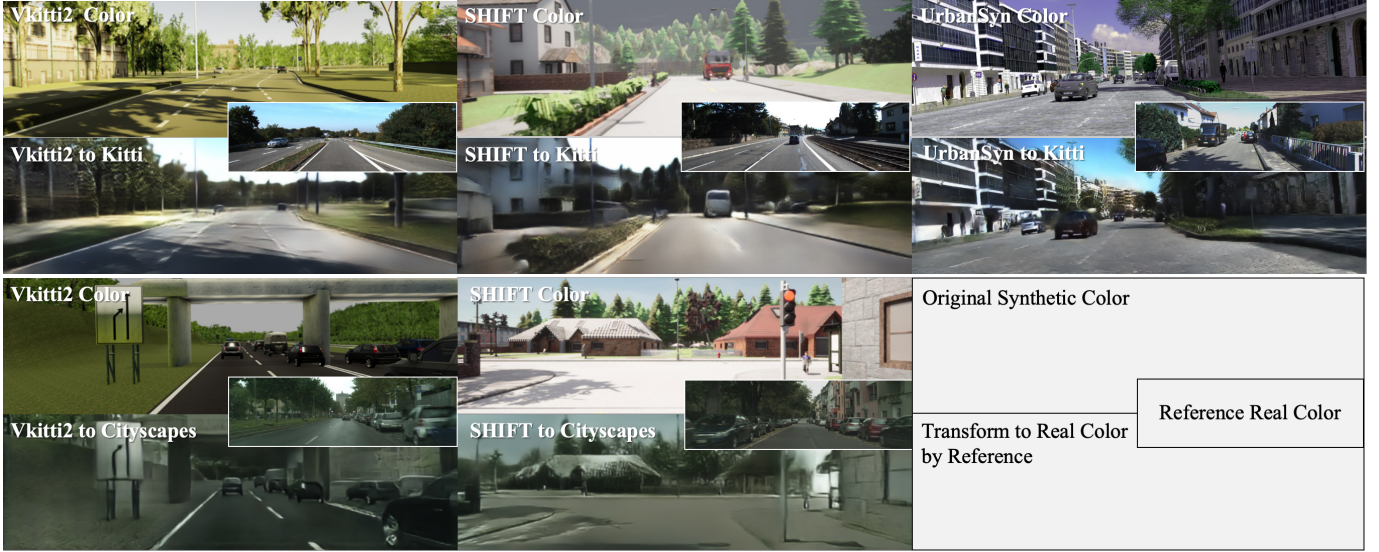


Fig. 3. **Color transformation for specific datasets**: Row 1 shows the reference color from the real-world dataset, Row 2 represents the color in the synthetic dataset, and Row 3 displays the synthetic-to-real transformation results.

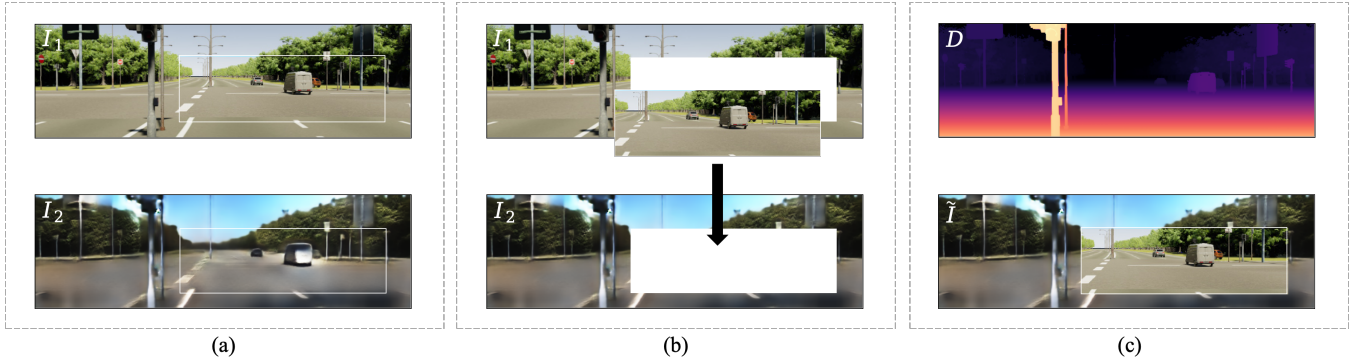


Fig. 4. **Syn-Real CutMix**: The specific steps of our Syn-Real CutMix method in spatially combining colors. (a) Randomly select a rectangular region  $M$ . (b) Replace the block in  $I_2$  with the blocks of  $I_1$ . (c) Form the new paired data  $(\tilde{I}, D)$ .

Objectively speaking, predicting color from 3D structural information constitutes a one-to-many mapping, a non-standard conditional generative tasks, where the same 3D structure can correspond to a multitude of different color images. However, under specific conditions, this seemingly impossible task becomes feasible: *Assuming that the color images in the target domain exhibit relatively high correlation.* The colors in real word datasets like Cityscapes and Kitti are notably different, as shown in Fig.3. Therefore, in order to bridge the substantial gap between synthetic  $\mathcal{S} \in \{\text{vKitti2 [10](Vk), SHIFT [45](S), UrbanSyn [46]}\}$  and real-world  $\mathcal{X} \in \{\text{Kitti [17], [47](K), Cityscapes [9](Cs)}\}$  datasets, we can learn the depth-to-color mapping in the source domain (real world color) and apply it to the target domain (synthetic color), thereby converting the target domain color to match those in the source domain. And then, we made the following attempts, train a Color Net  $\mathcal{F}_{d2c}$  to predict color images  $\hat{I}^{\mathcal{X}}$  from predicted depth images  $\hat{D}^{\mathcal{S}}$ :

$$\hat{I}^{\mathcal{X}} = \mathcal{F}_{d2c}(\hat{D}^{\mathcal{S}}|\theta^{\mathcal{X}}) \quad (1)$$

And utilizing the input of the Depth Net  $I^{\mathcal{X}}$  for Sup:

$$\mathcal{L}^{d2c} = pe(\hat{I}^{\mathcal{X}}, I^{\mathcal{X}}) \quad (2)$$

Here,  $\theta^{\mathcal{X}}$  represents the weights that store specific dataset color mapping information, such as Kitti and Cityscapes. Fortunately, we found that this prediction is feasible, neural networks are able to capture color information under specific target scenes. Next, we need to investigate whether we can employ  $\theta^{\mathcal{X}}$  to convert predicted  $\hat{D}^{\mathcal{S}}$  in synthesized datasets into color that resemble the Kitti( $\mathcal{X}$ ) color style: **Using the specific Color Net to colorize predicted synthetic depth**, as shown in Fig.3:

$$\hat{I}^{\mathcal{S} \rightarrow \mathcal{X}} = \mathcal{F}_{d2c}(\hat{D}^{\mathcal{S}}|\theta^{\mathcal{X}}) \quad (3)$$

2) *Syn-Real CutMix*: the renowned augmentation technique CutMix [18], replaces removed pixels with patches from other images rather than simply removing them. This strategy eliminates uninformative pixels during training, enhancing efficiency, while maintaining the advantages of regional dropout to focus on non-discriminative obstacle parts. Additionally, introducing extra patches improves the model's localization

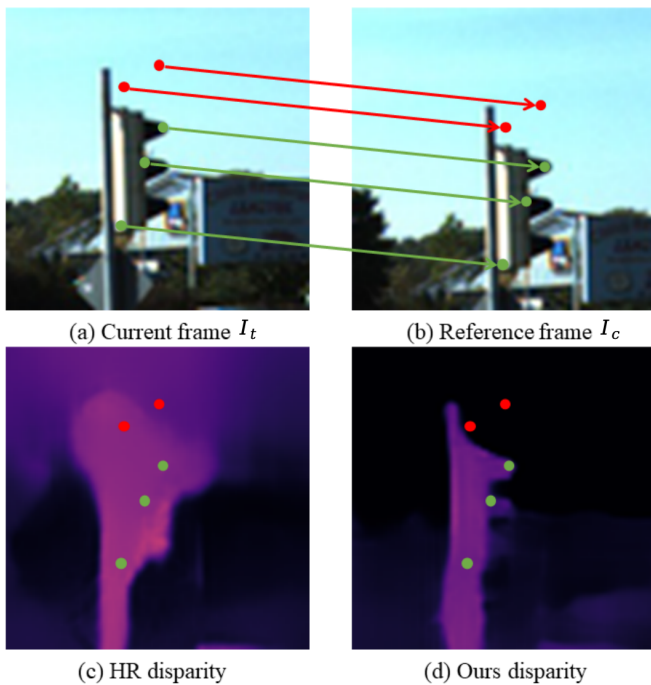


Fig. 5. **Chaotic depth clouds**: The green line can be matched across relevant frames based on the features of foreground obstacle, while the red line lacks effective features for matching, resulting in a cloud-like region in the depth image.

ability, requiring identification of obstacles from partial views. In our work, we apply this technique to jointly train both real-world and synthetic datasets, named **Syn-Real CutMix**.

The goal of CutMix in our work is to generate a new training pair  $(\tilde{I}, D)$ . Unlike CutMix [18], our samples  $(I^S, \tilde{I}^{S \rightarrow \mathcal{X}})$  are not two unrelated samples; instead, they correspond to different colored images of the same depth label  $D^S$ . Therefore, we only need to merge color images without combining new labels for them. To increase the randomness of training samples. As shown in Fig.4, given image samples  $(I^S, \tilde{I}^{S \rightarrow \mathcal{X}})$  as  $(I_1, I_2)$ , we firstly randomly swap  $(I_1, I_2)$ . Then, randomly crop a block from  $I_1$  with a height and width greater than half of the original image, and replace it with the corresponding position in  $I_2$ :

$$\tilde{I} = M \odot I_1 + (1 - M) \odot I_2 \quad (4)$$

where  $M \in \{0, 1\}$  denotes a binary mask indicating where to drop out and fill in, and  $\odot$  is element-wise multiplication.

Now, we combine Syn-Real enhanced images  $\tilde{I}$  and Real world target image  $I$  into one batch for training. Then, we can train monocular depth estimation networks simultaneously on real-world, synthetic, and Syn-to-Real images within a batch. Spatial randomization also encourages the network to focus more on the image structure rather than its specific colors.

3) *Background textureless regularization loss*: when analyzing and comparing unsupervised monocular depth and synthesized depth, we found not only significant gap in color images but also substantial gaps in the depth outputs generated by the model. In Fig.5, when the background of obstacle is textureless regions, these areas lack features for matching in sequences or stereo, making it challenging to accurately

determine their depth. Consequently, these regions are prone to arbitrary depth assignments within the textureless area, leading to the formation of cloud-like regions in the depth map, we called them chaotic depth clouds. The main drawback of such cloud-like regions lies in their ability to significantly impact the overall distribution of depth values in the depth map, resulting in notable biases when calculating median variance during evaluation processes.

For chaotic depth clouds, they appear mostly within regions with the sky as background, such as trees, road signs, and buildings. Fortunately, the sky's depth itself has a strong prior, that it is infinitely far away. Therefore, we predict the mask of the sky and constrain its value on the disparity map estimation by the network. This ensures that the network separates background and foreground obstacles:

$$\mathcal{L}^{sky} = \frac{\sum |M_{sky} \times \hat{D}|}{\sum M_{sky}} \quad (5)$$

Here,  $M_{sky}$  is inferred from a pre-trained semantic segmentation network [48]. We also have an intuitive prior that the sky should only exist above in the view, so we added a decay coefficient  $d$  that decreases with the image height:

$$d[\dots, j] = (H - j)/H \quad (6)$$

where  $H$  is the height of  $D_t$ , so our final sky regularization loss function is:

$$\mathcal{L}^{sky} = \frac{\sum d \times |M_{sky} \times \hat{D}|}{\sum M_{sky}} \quad (7)$$

The proposed sky regularization loss effectively eliminates hazy depth and, at the same time, enhances the recovery of delicate obstacles.

## B. Vision Attention Depth Net

Every high-performing depth estimation network requires an effective and robust backbone to extract hierarchical features from natural images. Commonly used backbones include ResNet [49] (Monodepth2 [8], HRDepth [25], CADepth [24]), HRNet [50] (DIFFNet [26], RA-Depth [27]), and Transformer-based backbones like ViT [29], MPViT [35](MonoViT [33], TUSDepth [20]). With the evolution from ResNet to HRNet and then to Transformer-based approaches, the performance of depth estimation continues to improve, but accompanied by increasing computational complexity and params. We consistently believe that depth estimation tasks, especially those based on street scenes, need to consider the requirements of their usage scenarios (real-time, lightweight). Hence, we aim to find a more efficient and effective backbone than Transformer methods.

Research on balancing the performance and efficiency of CNN and Transformer models has been ongoing, and we have discovered the VAN [19] (Vision-Attention-Network) model. The VAN [19] model employs large kernel convolutions instead of self-attention mechanisms to capture long-range dependencies. As shown in Fig.6, It decomposes the large kernel convolution into a spatial local convolution (depth-wise convolution), a spatial long-range convolution (depth-wise dilation convolution), and a channel convolution ( $1 \times 1$

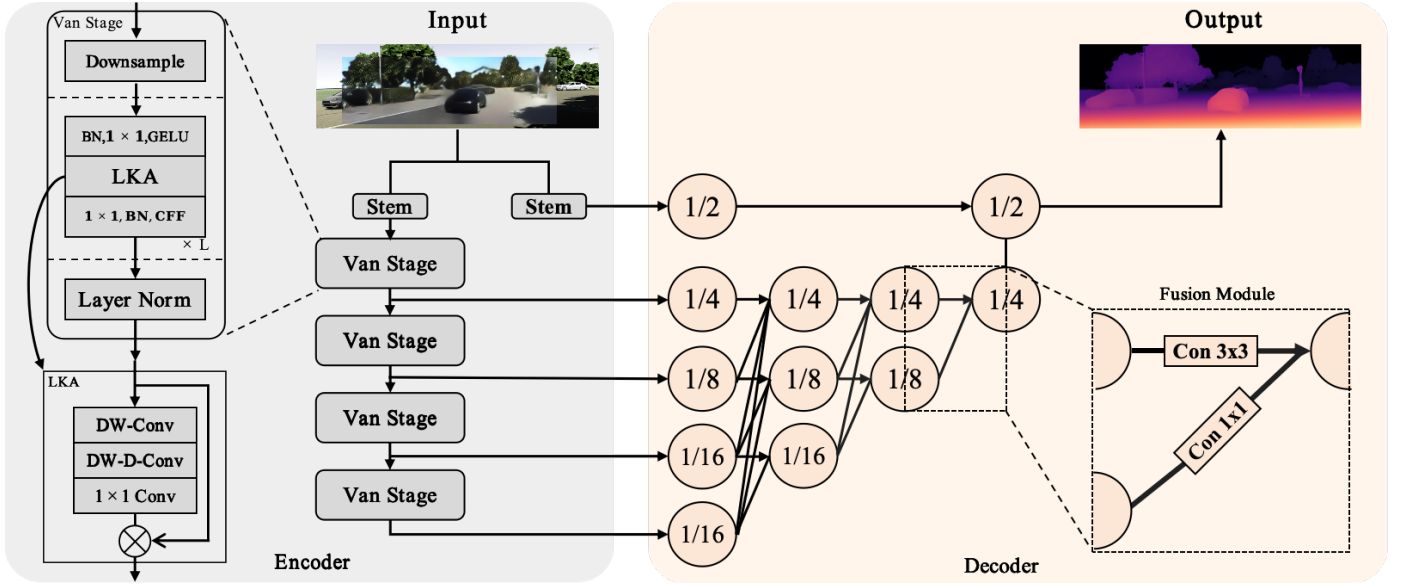


Fig. 6. The depth estimation network we designed based on the Vision Attention Network. The encoder is composed of an ImageNet pretrained Vision Attention Network (VAN), generating multi-scale features. The VAN stages consist of the Large Kernel Attention (LKA) module, which is purely a CNN structure. This encoder balances performance and efficiency. The decoder features an HRNet structure, where each stage fuses multiple scales of features upward.

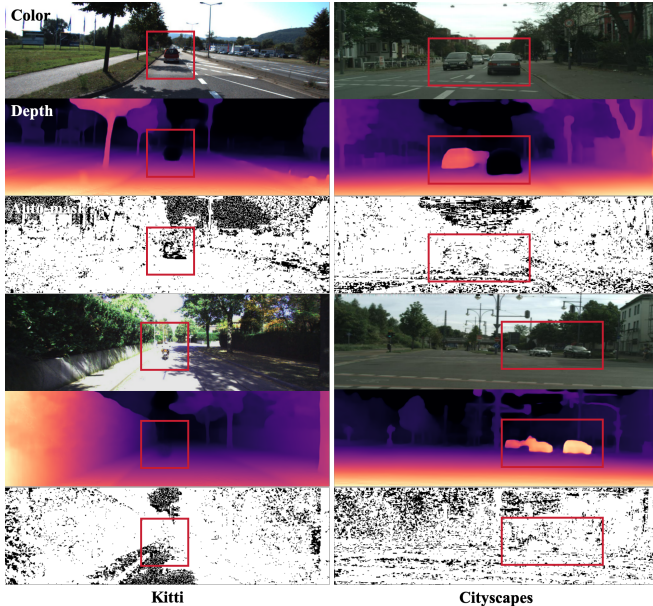


Fig. 7. When network capabilities become stronger, and the number of non-rigid objects in the dataset increases, the shortcomings [20] of Auto-masking and Minimum Reprojection Error lead to the reappearance of errors.

convolution) to reduce computational complexity. This design not only avoids treating 2D images as 1D sequences but also achieves stronger accuracy on ImageNet while reducing computational complexity and params.

Due to its outstanding performance and efficiency, we have introduced the VAN model into unsupervised monocular depth estimation tasks, and adapt to some fine-tuning. The most significant change is that, to reduce computational complexity, VAN downsamples the input resolution to  $2^{-2}$  during the first stem stage. While this downsampling is acceptable for

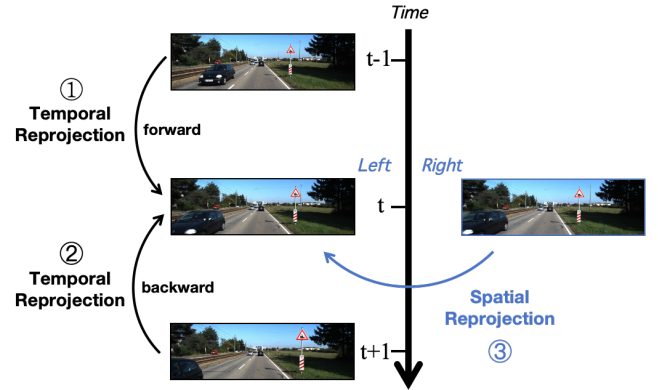


Fig. 8. Temporal reprojection involves reprojecting the previous and subsequent frames to the target frame, while spatial reprojection involves reprojecting the left or right frame to the target frame.

classification tasks, it poses challenges for high-resolution recovery in image regression tasks. Therefore, without altering the original VAN structure, we have added an additional stem head to acquire features at  $2^{-1}$  resolution, as shown in Fig.6. After extracting features from various VAN stages, we equipped them with a high-resolution depth decoder [27] to output the final depth. During implementation, we observed no difference between outputting a single-size depth image and outputting multi-scale depth images. Therefore, our network only outputs depth maps that are the same size as the input images.

### C. Auto-learning uncertainty temporal-spatial fusion

When testing our designed VADepth model, we found that the Auto-masking method almost failed, as shown in Fig.7. This issue is more severe in the Cityscapes [9]. Upon

inspecting the output of Auto-masking, we discovered that it couldn't perfectly shield non-rigid objects. We attribute this to the model's robustness, the limitations of the Auto-masking method, and the complexity of the Cityscapes [9], [51].

Therefore, we need to address the issue of non-rigid objects to further enhance performance. In temporal sequential frames, there are freely moving targets, such as pedestrians and vehicles (as show in Fig.8). These do not conform to the rigid scene transformation assumptions based on depth and camera pose. The solution provided by Auto-Masking [8] is to compare the pixels before and after reprojection. If the reprojection error after reprojection is worse than without reprojection, it indicates that the pixel belongs to a non-rigid object.

$$\mu = [\min_c pe(I_t, I_{c \rightarrow t}) < \min_c pe(I_t, I_c)]. \quad (8)$$

However, the network can still rationalize the depth of non-rigid moving objects by pulling forward targets further away and pushing backward closer targets, making them consistent with the camera extrinsics (Pose), as show in Fig.7. In fact, non-rigid moving objects only exist in temporally related frames, while in spatially related frames (stereo settings), since they are captured at the same moment, this issue does not arise. Therefore, introducing stereo supervision into the system is the most direct and effective method, rather than merely excluding masks for non-rigid objects [8], [51].

But when comparing temporal sequence reprojection with spatial reprojection, each has its own advantages and disadvantages. First, the translation of pose between temporally related frames are larger, whereas in spatial reprojection (stereo), the baseline is fixed and small. This makes temporal-based transformations better suited for estimating distant targets. Then, temporally related frames typically include three frames: the current frame and the preceding and following frames, allowing information from the preceding and following frames to fill in occluded areas in the target frame. In spatial reprojection (stereo), regardless of whether the target frame is set as the left or right eye, there is no symmetric completion of occluded areas. Thus, we seek a method that can effectively combine the advantages of both temporal and spatial reprojections to predict better depth maps.

In the work by Zhu et al. [52], a method was introduced to address occlusion problems by automatically predicting uncertainty and reweighting the reprojection in the reprojection process of spatially adjacent frames. Building on this idea, we aim to take it a step further by introducing a method to predict uncertainty during both temporal and spatial reprojections. This approach seeks to leverage the strengths of both temporal and spatial domains effectively.

To combine photometric loss across different frames, they specify  $\sum_c (1 - \hat{u}_{i,c}) = 1, c \in \{t-1, t+1\}$ . Hence, they combine the output uncertainty map  $\hat{U}_c (\hat{U}_c \geq 0)$  with softmax:  $\{U_{t-1}, U_{t+1}\} = 1 - \text{Softmax}\{\hat{U}_{t-1}, \hat{U}_{t+1}\}$ , to ensure that  $\sum_c u_{i,c} = 1$ . The final joint optimization function is written as:

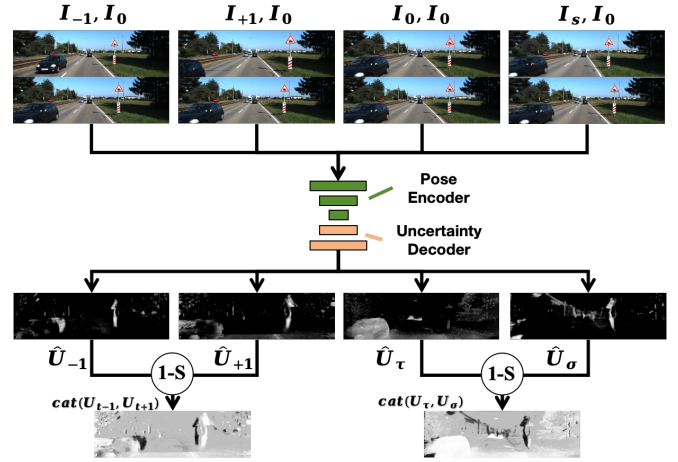


Fig. 9. **Auto-Spatio-Temporal Uncertainty Fusion:** The Uncertainty Generation Network utilizes a Pose Encoder and establishes an Uncertainty Decoder. It inputs the  $I_{\{-1,+1,0,s\}}$  and the target frame  $I_0$  separately to output the uncertainty map  $\hat{U}$ . Then, it generates the weight map  $U$  for different error maps through a **1-Softmax** operation.

$$\begin{aligned} \mathcal{L} = & \frac{1}{N} \sum \sum_c u_{i,c} pe_i(I_t, I_{c \rightarrow t}) \\ & + \alpha \frac{1}{N} \sum \hat{u}_{i,c}, \quad \sum_s u_{i,c} = 1 \end{aligned} \quad (9)$$

Using this formula, the network will automatically learn the uncertain regions within the loss, forming the final weights for multi-frame loss through comparison (areas where the loss cannot be reduced through optimization). In the temporal multi-frame reprojection loss combination, high-uncertainty regions are the occluded areas revealed due to reprojection. Meanwhile, in the process of spatial and temporal reprojection loss combination, high-uncertainty regions should be the non-rigid motion areas that temporal reprojection cannot resolve.

$$\begin{aligned} \mathcal{L}^{uD} = & \frac{1}{N} \sum \left( u_{i,\tau} \sum_c u_{i,c} pe_i(I_t, I_{c \rightarrow t}) + u_{i,s} pe_i(I_t, I_{s \rightarrow t}) \right) \\ & + \alpha \frac{1}{N} \sum \hat{u}_{i,\theta}, \quad \theta \in \{-1, +1, \tau, s\} \end{aligned} \quad (10)$$

$\tau$  and  $s$  represent the temporal domain and the spatial domain, respectively.  $u_{i,\tau}$  and  $u_{i,s}$  represent the temporal-domain uncertainty and the spatial-domain uncertainty,  $\sum_s u_{i,c} = 1, u_{i,\tau} + u_{i,s} = 1, \{U_\tau, U_s\} = 1 - \text{Softmax}\{\hat{U}_\tau, \hat{U}_s\}$ .  $s$  represents the source frame in a stereo setup. Since the Kitti dataset randomly selects either the left or right camera image as the target frame, the other frame becomes the source frame.

Regarding how to obtain temporal and spatial uncertainty maps, we consider referencing the method used to generate temporal uncertainty maps by inputting related frames containing uncertainty information. For spatial reprojection, we can input  $I_s$  and  $I_0$ , but there is no single related frame that uniquely represents temporal reprojection. We attempt to input

$I_0$  and  $I_0$  as representatives. By comparing the output uncertainty maps when calculating the loss, we can form reasonable uncertainty maps, as shown in Fig. 9. Applying uncertainty learning in temporal reprojection can address occlusion and field contraction issues. We improved and applied this method to fuse temporal and spatial reprojection errors. Since non-rigid objects are rigid in the spatial domain, the temporal domain generates significant uncertainty. Additionally, high uncertainty still arises from occluded regions during the spatial domain reprojection process. By fusing the uncertainties from both the temporal and spatial domains, we can ignore high-uncertainty areas in each domain when calculating the loss, leveraging the strengths of each domain to train better depth images.

Applying uncertainty learning in temporal reprojection can address occlusion and field contraction issues [20]. We improved and applied this method to fuse temporal and spatial reprojection losses. Since no-rigid objects are rigid in the spatial domain, the temporal domain generates significant uncertainty, as shown in Fig. 10. Additionally, high uncertainty still arises from occluded regions during the spatial domain reprojection process. By fusing the uncertainties from both the temporal and spatial domains, we can ignore high-uncertainty areas in each domain when calculating the loss, leveraging the strengths of each domain to train better depth images, as shown in Fig. 9.

#### D. Training Strategy

1) *Synthetic supervised depth loss*: since unsupervised depth estimation models based on video sequences cannot recover scale information, in order to enable joint training with synthesized depth which has deterministic depth values, varying with different camera parameters, we adopt the same affine-invariant mean absolute error loss as MiDas [53] and Depth Anything [54]:

$$\mathcal{L}^{sD} = \frac{1}{HW} \sum_i |d_i^* - \hat{d}_i^*| \quad (11)$$

Here,  $d_i^*$  and  $\hat{d}_i^*$  are the scaled and shifted pixels of predicted  $\hat{D}$  and synthetic groundtruth  $D$ .

$$d_i^* = \frac{d_i - \text{median}(d)}{s(D)}, s(D) = \frac{1}{HW} \sum_i |d_i - \text{median}(d)| \quad (12)$$

2) *Optimization Strategy*: Swami et al. [36] highlighted that multiple networks and optimization losses in unsupervised domain adaptation methods often compete against each other and fail to contribute effectively to the optimization of the depth estimation task. This lack of cooperation among different components makes it challenging to achieve best results. So here, we have set two optimizers  $\{\mathcal{O}_{d2c}, \mathcal{O}_{d2e}\}$  to separately train the Depth Net and the Color net, as shown in Fig. 2.

**Optimizer 1- $\mathcal{O}_{c2d}$** : Supervised training of the Depth Net on the Syn-Real dataset and the Color Net on the Real world unsupervised depth dataset for predicting color from depth,  $\beta = 1.0, \alpha = 1e^{-3}$ .

$$\mathcal{L}^{\mathcal{O}_{d2c}} = \mathcal{L}^{d2c} + \beta \mathcal{L}^{sD} + \alpha \mathcal{L}^{sm} \quad (13)$$

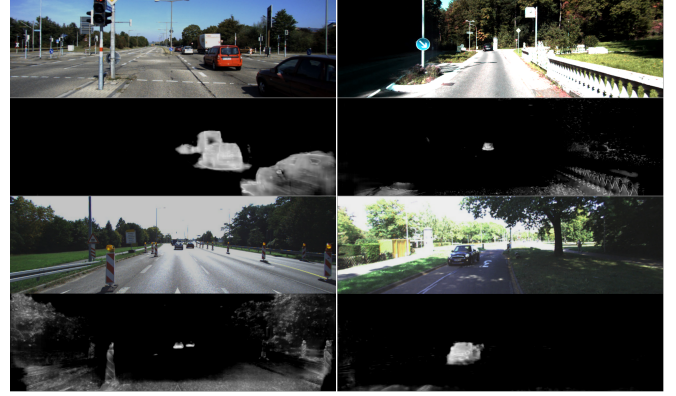


Fig. 10. **Temporal Uncertainty for no-rigid objects**: We can identify no-rigid objects by predicting the uncertainty during the training process, thereby eliminating their impact in the training. The fine-grained recognition can even identify very small non-rigid targets.

**Optimizer 2- $\mathcal{O}_{c2d}$** : Unsupervised training of the Depth Net on the Real world unsupervised depth dataset and applied the background textureless regularization loss,  $\alpha = 1e^{-3}, \gamma = 1e^{-2}$ .

$$\mathcal{L}^{\mathcal{O}_{c2d}} = \mathcal{L}^{uD} + \alpha \mathcal{L}^{sm} + \gamma \mathcal{L}^{sky} \quad (14)$$

## IV. EXPERIMENTS

In this section, we initially establish the superiority of our Back2Color by comparing it with other state-of-the-art (SoTA) approaches on the KITTI Eigen split and Cityscapes depth estimation benchmark (Tab.III, Tab.IV, and Tab.I). Following this, we conduct ablation experiments to analyze the effects of the proposed methods (Tab.VII and Tab.VI). Additionally, we compare our approach with other methods that utilize synthetic datasets (Tab.II), perform comparisons at higher resolutions (Tab.V), and benchmark against the lightest and most effective methods (Tab.VIII). At the same time, we present some visual results of our method on the KITTI and Cityscapes datasets (Fig. 12, Fig. 15, and Fig. 16).

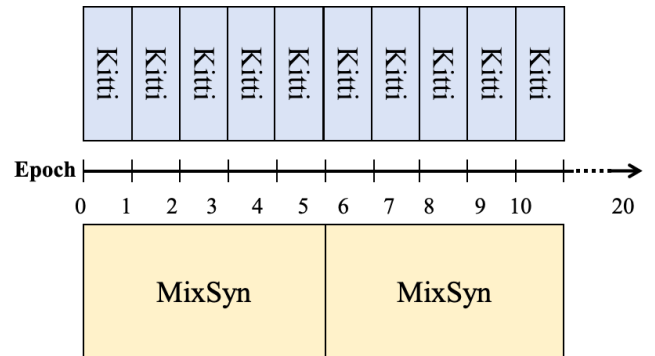


Fig. 11. **The MixSyn dataset** contains more samples compared to the real-world unsupervised datasets, necessitating the division of the MixSyn dataset into multiple epochs. While the MixSyn dataset is trained through once, the real-world datasets may undergo multiple training passes.

## A. Datasets

We utilized two unsupervised monocular depth estimation datasets: KITTI [47] and Cityscapes [9], along with synthetic datasets vKitti2 [10], SHIFT [45] and UrbanSyn [46]. **KITTI** consists of 39,810 training triplets, with 4,424 for validation and 697 for evaluation. It presents diverse scenes with rich color compositions and sporadic non-rigid objects. **Cityscapes**, tailored for autonomous driving, provides 69,731 monocular triplets from the LeftImg8bit Sequence for training. Primarily urban, it encompasses non-rigid pedestrians and vehicles, often depicted with darker color tones. When using stereo data from the KITTI and Cityscapes datasets, it is important to note that the baseline for KITTI is 54 cm, while for Cityscapes it is 22 cm. **vKitti2**, an upgraded version of Virtual KITTI, employs the Unity game engine to offer a more photorealistic environment. It provides diverse data types for various computer vision tasks, with 21,260 frames extracted for training. **SHIFT**, featuring various weather conditions and times, offers dense depth information with a 1 mm resolution and includes simulated pedestrians. We selected 153,000 frames and corresponding synthetic depths from its front-view cameras as our reference synthetic dataset. **UrbanSyn** [46], designed to address the synth-to-real domain gap, contributes to unprecedented synthetic-only baselines used by domain adaptation (DA) methods. It offers 7,539 images along with depth labels, providing a highly realistic synthetic dataset for various computer vision tasks.

To leverage the variety of multiple synthetic datasets, we normalized and shuffled the specifications (size, depth resolution, etc.) of the vKitti2, SHIFT, and UrbanSyn datasets to create a unified dataset called **MixSyn**. The MixSyn dataset contains significantly more samples compared to KITTI and Cityscapes. Therefore, during the training process, MixSyn is trained once, while KITTI or Cityscapes is trained for multiple epochs, as shown in Fig.11. We demonstrate the advantages of using MixSyn in Tab. VII.

## B. Implementation Details

Our training is implemented by Pytorch [55] with NVIDIA RTX 3090Ti(24GB). We have used ADAM [56] as the optimizer. We have set the learning rate to  $1 \times 10^{-4}$ , the same as in Monodepth2 [8], and the learning rate will decay to  $1 \times 10^{-5}$  after 15 epochs. The other parameters are the same as  $(\beta_1, \beta_2) = (0.9, 0.999)$ . We set the SSIM weight to  $\alpha = 0.85$  and the smoothness weight to  $\lambda = 1e - 3$ . Furthermore, we utilized a pretrained segmentation network [48] trained on the Cityscapes semantic segmentation dataset. We evaluate the performance using depth estimation metrics [47]:  $rmse(\log)$ ,  $rmse$ , Sq.relative, Abs relative, and Accuracy.

## C. Monocular Depth Estimation Performance

Our recommended experimental setup is to use the VAN2 model (balancing efficiency and performance), utilize the MixSyn synthetic dataset, and employ spatiotemporal supervision (ms). If there are no annotations, the results should be based on this setup. The evaluation results are summarized

TABLE I  
EXPERIMENTS ON THE CITYSCAPES BENCHMARK WITH  $192 \times 640$ .  
METHODS\* REQUIRING SEMANTIC INFORMATION AND BACK2COLOR  
REQUIRING STEREO SET.

Method	Error Metric				Accuracy Metric		
	abs_rel	sq_rel	rmse	rmse_log	a1	a2	a3
<b>Struct2Depth*</b> [57]	0.145	1.737	7.280	0.205	0.813	0.942	0.976
<b>GLNet</b> [58]	0.129	1.044	5.361	0.212	0.843	0.938	0.976
<b>Gordon et al.*</b> [59]	0.127	1.330	6.960	0.195	0.830	0.947	0.981
<b>Li et al.</b> [60]	0.119	1.290	6.980	0.190	0.846	0.952	0.982
<b>Lee et al.*</b> [61]	0.111	1.158	6.437	0.182	0.868	0.961	0.983
<b>RM-Depth</b> [51]	0.090	0.825	5.503	0.143	0.913	0.980	0.993
<b>Back2color*</b>	<b>0.076</b>	<b>0.784</b>	<b>5.159</b>	<b>0.127</b>	<b>0.937</b>	<b>0.984</b>	<b>0.994</b>

TABLE II  
EXPERIMENTS WITH METHODS USING THE SYNTHETIC DATASET  
(vKITTI2) AT  $192 \times 640$  RESOLUTION AND TRAINING WITH MONOCULAR  
SEQUENTIAL ONLY.

Method	Size	Error Metric				Accuracy Metric		
		abs_rel	sq_rel	rmse	rmse_log	a1	a2	a3
<b>MonoDEVSNet</b> [16]	<b>192x640</b>	0.102	<b>0.685</b>	<b>4.303</b>	0.178	0.894	0.966	<b>0.984</b>
<b>Back2Color</b>	<b>192x640</b>	<b>0.096</b>	0.708	4.307	<b>0.173</b>	<b>0.905</b>	<b>0.968</b>	<b>0.984</b>
<b>Swami et al.</b> [36]	<b>320x1024</b>	0.103	<b>0.654</b>	4.300	0.178	0.891	0.966	0.984
<b>Back2Color</b>	<b>320x1024</b>	<b>0.093</b>	0.687	<b>4.171</b>	<b>0.168</b>	<b>0.912</b>	<b>0.970</b>	<b>0.985</b>

in Tab.III and Tab.IV with Kitti Eigen Split [47] and Tab.I with Cityscapes benchmark, followed by an illustration of their performance qualitatively in Fig.12 and Fig.15. Our method outperforms all existing SoTA unsupervised approaches, including some based on transformer [33], [34] with larger params and more complex structures(Tab.VIII).

## D. Ablation Study

As illustrated in Tab. VI, we conducted experiments on our Back2Color framework by replacing different model structures to demonstrate the effectiveness of our method. While the Depth Net learned to predict dense depth from synthetic data, it also disrupted the model’s latent memory in unsupervised learning and learned to generate sharp boundaries of obstacles. Based on the metrics in Tab. VI, there is an improvement across all metrics, particularly the  $a1$  and  $rmse\_log$  metrics representing detail accuracy. At the same time, we also observed that there was no significant difference between using SHIFT and vKitti2. In Tab. VI, we also tested training VADepth from scratch without ImageNet pre-training. The results demonstrated that using a pre-trained checkpoint enhances the network’s ability to process natural images, significantly benefiting depth estimation.

And then, we compared our method with two other noval approaches also joint training with synthetic datasets. Our improvement remains significant in comparison, as shown in Tab.II.

Additionally, we used various synthetic datasets such as vKitti2, SHIFT, and UrbanSyn to real-world unsupervised depth model training, as shown in Tab.VII. The results consistently achieved excellent improvement, demonstrating the strong adaptability of our method. To demonstrate that the improvement in our Back2Color method is not due to the increased training samples (Synthetic Datasets) but rather due to the diverse priors brought by various synthetic datasets, we

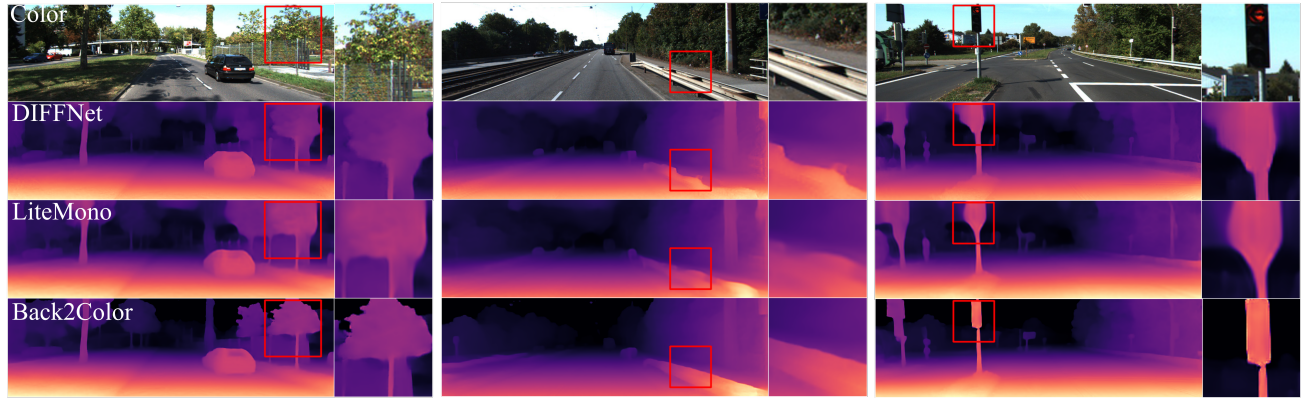


Fig. 12. **Visual of Depth Estimation on Kitti:** Our method yields clearer depth estimates with higher correlation to corresponding colors, sharper boundaries, and fewer areas with chaotic depth clouds.

TABLE III  
EXPERIMENTS ON THE KITTI EIGEN SPLIT USING ONLY THE MONOCULAR SEQUENCE DATASET FOR TRAINING.

Method	Sup.	Size	Error Metric				Accuracy Metric		
			abs_rel	sq_rel	rmse	rmse_log	a1	a2	a3
Monodepth2 [8]	m	192x640	0.115	0.903	4.863	0.193	0.877	0.959	0.981
CADepth [24]	m	192x640	0.105	0.769	4.535	0.181	0.892	0.964	0.983
DIFFNet [26]	m	192x640	0.102	0.749	4.445	0.179	0.897	0.965	0.983
MonoFormer [62]	m	192x640	0.106	0.839	4.627	0.183	0.889	0.962	0.983
Lite-Mono [34]	m	192x640	0.101	0.729	4.454	0.178	0.897	0.965	0.983
MonoViT [33]	m	192x640	0.099	0.708	4.372	0.175	0.900	0.967	<b>0.984</b>
Back2Color	m	192x640	<b>0.096</b>	<b>0.708</b>	<b>4.307</b>	<b>0.173</b>	<b>0.905</b>	<b>0.968</b>	<b>0.984</b>
DIFFNet [26]	m	320x1024	0.097	0.722	4.345	0.174	0.907	0.967	0.984
Lite- [34]	m	320x1024	0.097	0.710	4.309	0.174	0.905	0.967	0.984
MonoViT [33]	m	320x1024	0.096	0.714	4.292	0.172	0.908	0.968	0.984
Back2Color	m	320x1024	<b>0.093</b>	<b>0.687</b>	<b>4.171</b>	<b>0.168</b>	<b>0.912</b>	<b>0.970</b>	<b>0.985</b>

TABLE IV  
EXPERIMENTS ON THE KITTI EIGEN SPLIT USING ONLY THE MONOCULAR SEQUENCE AND STEREO DATASETS FOR TRAINING.

Method	Sup.	Size	Error Metric				Accuracy Metric		
			abs_rel	sq_rel	rmse	rmse_log	a1	a2	a3
Monodepth2 [8]	ms	192x640	0.106	0.818	4.750	0.196	0.874	0.957	0.979
HR-Depth [25]	ms	192x640	0.107	0.785	4.612	0.185	0.887	0.962	0.982
CADepth [24]	ms	192x640	0.102	0.752	4.504	0.181	0.894	0.964	0.983
DIFFNet [26]	ms	192x640	0.101	0.749	4.445	0.179	0.898	0.965	0.983
MonoViT [33]	ms	192x640	0.098	0.683	4.333	0.174	0.904	0.967	<b>0.984</b>
Back2Color	ms	192x640	<b>0.092</b>	<b>0.685</b>	<b>4.229</b>	<b>0.170</b>	<b>0.911</b>	<b>0.968</b>	<b>0.984</b>
Monodepth2 [8]	ms	320x1024	0.106	0.806	4.630	0.193	0.876	0.958	0.980
HR-Depth [25]	ms	320x1024	0.101	0.716	4.395	0.179	0.894	0.966	0.983
CADepth [24]	ms	320x1024	0.096	0.694	4.264	0.173	0.908	0.968	0.984
MonoViT [33]	ms	320x1024	0.093	0.671	4.202	0.169	0.912	0.969	0.984
Back2Color	ms	320x1024	<b>0.087</b>	<b>0.644</b>	<b>4.079</b>	<b>0.166</b>	<b>0.920</b>	<b>0.970</b>	<b>0.985</b>

conducted experiments using 20% and 50% synthetic samples (Rows 6, 7, and Rows 9, 10) while ensuring the total number of dataset samples remains the same as the KITTI dataset (39,810). The results are consistent with those obtained using the full dataset, proving that the enhancement of our method

TABLE V

EXPERIMENTS ON THE KITTI EIGEN SPLIT AT 384 × 1280 RESOLUTION.

Method	Sup.	Error Metric				Accuracy Metric		
		abs_rel	sq_rel	rmse	rmse_log	a1	a2	a3
PackNet-SfM [23]	m	0.107	0.802	4.538	0.186	0.889	0.962	0.981
SGDepth [63]	m	0.107	0.768	4.468	0.186	0.891	0.963	0.982
MonoViT [33]	m	0.094	0.682	4.200	0.170	0.912	0.969	0.984
PlaneDepth [64]	ms	0.090	<b>0.584</b>	4.130	0.182	0.896	0.962	0.981
Back2Color	ms	<b>0.086</b>	0.629	<b>4.054</b>	<b>0.165</b>	<b>0.920</b>	<b>0.970</b>	<b>0.985</b>



Fig. 13. **Temporal-Spatial Uncertainty Fusion:** White represents higher reliability in spatial reprojection, while black represents higher reliability in temporal reprojection, as shown in the legend in the bottom right corner. We can observe that non-rigid moving objects in the image tend to reproject more in space (white). Meanwhile, occluded areas and distant regions tend to reproject more in the temporal sequence (black), and the remaining areas show no significant tendency (gray).

TABLE VI  
EXPERIMENTS ON THE KITTI EIGEN SPLIT AT 192×640 RESOLUTION WITH DIFFERENT MODELS FOR BACK2COLOR.VAN\* MEANS NOT APPLY IMAGENET PRETRAINED CHECKPOINTS.

Method	Model	Error Metric				Accuracy Metric		
		abs_rel	sq_rel	rmse	rmse_log	a1	a2	a3
Monodepth2 [8]	Resnet34	0.106	0.818	4.750	0.196	0.874	0.957	0.979
Back2Color	Resnet34	<b>0.104</b>	<b>0.808</b>	<b>4.617</b>	<b>0.186</b>	<b>0.883</b>	<b>0.962</b>	<b>0.982</b>
HRDepth [25]	HRDepth	0.107	0.785	4.612	0.185	<b>0.887</b>	0.962	0.982
Back2Color	HRDepth	<b>0.105</b>	<b>0.745</b>	<b>4.469</b>	<b>0.182</b>	<b>0.887</b>	<b>0.964</b>	<b>0.984</b>
DIFFNet [26]	DIFFNet	0.101	0.749	4.445	0.179	0.898	0.965	0.983
Back2Color	DIFFNet	<b>0.094</b>	<b>0.660</b>	<b>4.254</b>	<b>0.172</b>	<b>0.904</b>	<b>0.967</b>	<b>0.984</b>
Back2Color	VAN2*	0.123	0.997	4.996	0.202	0.858	0.953	0.979
Back2Color	VAN2	<b>0.092</b>	<b>0.685</b>	<b>4.229</b>	<b>0.170</b>	<b>0.911</b>	<b>0.968</b>	<b>0.984</b>

is not due to the increase in training samples. Additionally, when using the MixSyn mixed synthetic dataset, some metrics (rmse\_log and a1) show significant improvement compared to using a single synthetic dataset, demonstrating that our method benefits from learning the variety of multiple synthetic datasets.

Finally, to demonstrate the exceptional efficiency of our model, we compared it with the current best-performing MonoViT [33] and the lightweight Lite-mono [34]. Our VAN0

TABLE VII  
ABLATION STUDY ON THE IMPACT OF VARIOUS SYNTHETIC DATASETS.

Size	Syn	Number of Samples				Error Metric				Accuracy Metric		
		Kitti	vKitti2	SHIFT	UrbanSyn	abs_rel	sq_rel	rmse	rmse_log	a1	a2	a3
192x640	vKitti2	39810	21260	0	0	0.094	0.694	4.296	0.173	0.907	0.968	0.984
192x640	SHIFT	39810	0	153000	0	<b>0.092</b>	0.676	4.238	0.171	0.909	<b>0.969</b>	0.984
192x640	Urban	39810	0	0	7539	0.093	<b>0.644</b>	<b>4.198</b>	0.172	0.907	0.968	0.984
192x640	MixSyn	39810	21260	153000	7539	<b>0.092</b>	0.685	4.229	<b>0.170</b>	<b>0.911</b>	0.968	0.984
320x1024	vKitti2	39810	21260	0	0	0.090	0.677	4.173	0.169	0.914	0.969	0.984
320x1024	vKitti2	31848	7962	0	0	0.090	0.675	4.143	0.168	0.917	0.970	0.985
320x1024	vKitti2	19905	19905	0	0	0.091	0.684	4.192	0.169	0.913	0.969	0.985
320x1024	SHIFT	39810	0	153000	0	0.089	0.651	4.158	0.167	0.916	0.970	0.985
320x1024	SHIFT	31848	0	7962	0	0.090	0.684	4.158	0.168	0.916	0.970	0.984
320x1024	SHIFT	19905	0	19905	0	0.090	0.680	4.144	0.167	0.915	0.970	0.985
320x1024	Urban	39810	0	0	7539	0.090	0.654	4.084	0.167	0.915	0.970	0.985
320x1024	MixSyn	39810	21260	153000	7539	<b>0.087</b>	<b>0.644</b>	<b>4.079</b>	<b>0.166</b>	<b>0.920</b>	0.970	0.985



Fig. 14. **The synthetic datasets:** In vKitti2, depth cannot penetrate transparent entities such as glass windows, whereas in the SHIFT dataset, depth can penetrate transparent entities. SHIFT and UrbanSyn includes simulated pedestrians. And UrbanSyn is the synthetic dataset that most closely resembles real world.

model is not only lighter than Lite-mono but also delivers superior performance. Additionally, it achieves competitive results with only one-sixth of the parameters of MonoViT. Meanwhile, our VAN2 model, which has a parameter count similar to MonoViT, shows a significant performance improvement, making it the current state-of-the-art (SOTA) model.

### E. Visualization Analysis

The impact of synthetic datasets on real-world unsupervised depth estimation can be analyzed by comparing the joint training with different synthetic datasets, as shown in the Fig.16.

Firstly, it's undeniable that our method, through joint training with synthetic datasets, achieves clearer boundaries and more detailed depth estimations compared to training solely with unsupervised depth estimation, as depicted in Fig. 12.

The model successfully captures features of obstacles that unsupervised learning alone struggles to discern. For instance, roadside barriers (Fig.12, Col 2), which run parallel to the direction of vehicle movement and remain unchanged across multiple frames, pose challenges for unsupervised methods but are accurately predicted with the aid of synthetic depths. Synthetic depths are dense and accurate, providing crucial information about these obstacles.

Furthermore, the characteristics of synthetic datasets are also learned by the network. For example, as shown in Fig.14, the SHIFT dataset has two characteristics compared to the vKitti2. Firstly, it contains a amount of pedestrians, which are often difficult to estimate correctly in unsupervised depth estimation, typically resulting in partial depth disappearance or blurring, as seen in the estimation results of DIFFNet in the Fig.15, Row 1. When using our method with the SHIFT dataset, the network learns the knowledge of estimating pedestrian, achieving clear and accurate estimation of pedestrian depth, which is impressive.

This point can also be inferred from predicted depth of transparent objects, such as glass. As shown in Fig.14, in the vKitti2, transparent objects like glass are treated as solid entities and can be detected, resulting in smooth surfaces in Depth. However, in the SHIFT, transparent objects are considered penetrable targets, leading to discontinuous depth in these regions. This difference in Synthetic dataset definitions is perfectly reflected in the training, as shown in Fig.16, Row 2. Models trained with the SHIFT dataset recognize and penetrate through vehicle windows, whereas those trained with the vKitti2 dataset perceive them as flat surfaces.

### F. Discussion

1) *Why can the network transform information beyond depth:* in Fig. 3, Syn-to-Real images exhibit excessive detail surpassing depth information alone, such as tree shadows and lane markings. We attribute this to the Color-Depth-Color process, where depth, predicted from color, retains texture details (such as subtle gradient changes at some boundaries). Consequently, the Color network can recover such gradient changes from the depth map. To validate, we directly trained the network to predict color images from synthesized depth

TABLE VIII  
 ABLATION STUDY ON MODELS WITH PARAMS AND COMPUTATIONAL COMPLEXITIES(GFLOPS).

Method	Model	Size	Params(M)	Flops(G)	Error Metric				Accuracy Metric		
					abs_rel	sq_rel	rmse	rmse_log	a1	a2	a3
MonoViT	small	320x1024	33.63	159.14	0.093	0.671	4.202	0.169	0.912	0.969	<b>0.985</b>
Lite-mono	8M	320x1024	8.76	29.88	0.097	0.710	4.309	0.174	0.905	0.967	0.984
Back2Color	VAN0	320x1024	5.17	17.64	0.094	0.706	4.257	0.171	0.910	0.969	0.984
Back2Color	VAN1	320x1024	18.61	51.48	0.090	0.664	4.139	0.168	0.915	0.970	0.984
Back2Color	VAN2	320x1024	31.32	76.01	<b>0.087</b>	<b>0.644</b>	4.079	0.166	<b>0.920</b>	0.970	<b>0.985</b>
Back2Color	VAN3	320x1024	49.5	114.63	<b>0.087</b>	0.653	<b>4.068</b>	<b>0.165</b>	0.919	<b>0.971</b>	<b>0.985</b>
Back2Color	VAN0	384x1280	5.17	17.64	0.093	0.676	4.169	0.171	0.911	0.969	0.984
Back2Color	VAN1	384x1280	18.61	51.48	0.090	0.664	4.102	0.168	0.917	<b>0.970</b>	0.984
Back2Color	VAN2	384x1280	31.32	76.01	<b>0.086</b>	<b>0.629</b>	<b>4.054</b>	<b>0.165</b>	<b>0.920</b>	<b>0.970</b>	<b>0.985</b>
Back2Color	VAN3	384x1280	49.5	114.63	0.087	0.652	4.062	<b>0.165</b>	<b>0.920</b>	<b>0.970</b>	0.984

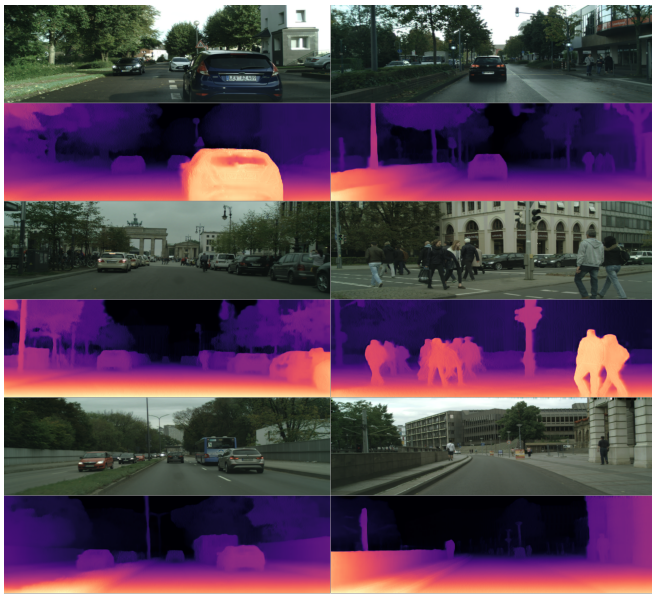


Fig. 15. **The visual results on Cityscapes:** Our method yields clearer depth estimates with higher correlation to corresponding colors, sharper boundaries, and fewer areas with chaotic depth clouds.

in the synthetic dataset (Fig. 17). The absence of lane markings and shadows in the restored color images confirms our hypothesis.

2) *Why learn Depth and Color Net simultaneously online:* the primary objective of our method is depth prediction. As the Depth Net undergoes continuous updates to enhance its accuracy and performance, it is imperative to ensure that the Color Net also adapts accordingly. This synchronization is crucial for achieving superior color transformation effects. By reprojecting the Color Net’s adjustments with the updates in the Depth Net, we aim to optimize the overall performance of the model. This dynamic adjustment process ensures that the color transformation remains effective and reproject with the evolving depth predictions.

3) *Can the VAN-based encoder replace the ResNet structure in the Pose encoder:* so far, we have not observed any new research that can replace the ResNet-based PoseEncoder [8], whether using CNN-based or Transformer-based methods. We have attempted some alternatives, but none have improved depth estimation performance; in fact, many have resulted in performance degradation. In this study, we also tried using a

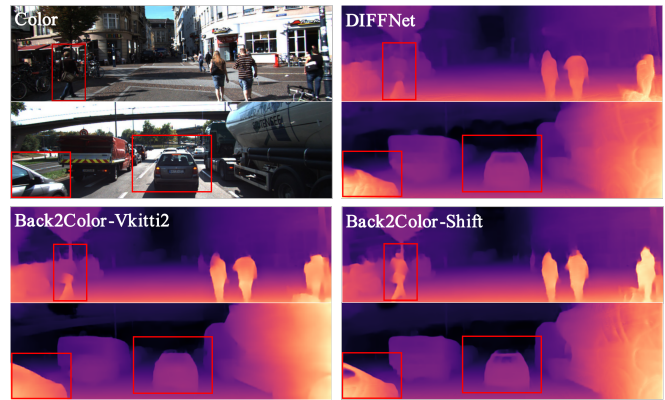


Fig. 16. The visual results of joint training with different synthetic datasets. The model trained with SHIFT jointly learns more features of pedestrians while treating glass as transparent entities.

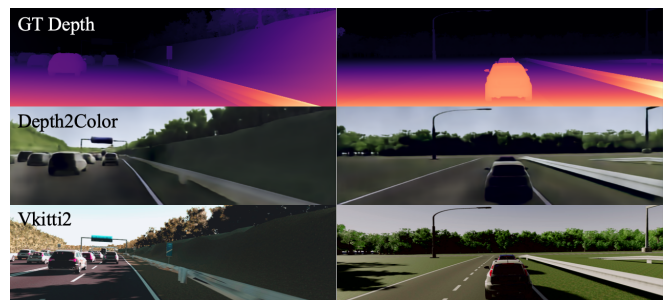


Fig. 17. An experiment predicting color from ground truth (GT) depth showed that shadows and road markings vanished, undetectable in the depth image. See Discussion for details.

VAN-based model to replace the ResNet-based PoseEncoder, but still did not observe any significant improvement. We believe that the pose estimation task is a small parameter regression task that is relatively simple compared to depth prediction and does not require a powerful network.

## V. CONCLUSION

In this paper, we presented Back to the Color (Back2Color), a novel method designed to enhance unsupervised depth estimation by leveraging synthetic data. Our method addresses the challenge of aligning synthetic depth information with real-world colors, enabling the transformation of predicted synthetic depth into realistic colors with high fidelity. By

joint training on synthetic and real-world datasets using Back2Color, we observed substantial improvements in depth estimation performance. Additionally, we designed a depth network based on the Vision Attention Network (VAN), which allowed our CNN-based network to surpass several Transformer-based depth models. Furthermore, we improved the uncertainty-based loss fusion method by combining the advantages of temporal and spatial reprojection, thoroughly addressing issues related to non-rigid motion. Experimental results demonstrated the effectiveness of our method on both the KITTI and Cityscapes datasets. Overall, Back2Color offers a promising solution for advancing unsupervised depth estimation by effectively integrating synthetic data into the training process.

## REFERENCES

- [1] C. B. Hochberg and J. E. Hochberg, "Familiar size and the perception of depth," *The Journal of Psychology*, vol. 34, no. 1, pp. 107–114, 1952.
- [2] S. Gokturk, H. Yalcin, and C. Bamji, "A time-of-flight depth sensor - system description, issues and solutions," in *2004 Conference on Computer Vision and Pattern Recognition Workshop*, 2004, pp. 35–35.
- [3] N. Li, C. P. Ho, J. Xue, L. W. Lim, G. Chen, Y. H. Fu, and L. Y. T. Lee, "A progress review on solid-state lidar and nanophotonics-based lidar sensors," *Laser & Photonics Reviews*, vol. 16, no. 11, p. 2100511, 2022.
- [4] Q.-T. Luong and O. D. Faugeras, "The fundamental matrix: Theory, algorithms, and stability analysis," *International journal of computer vision*, vol. 17, no. 1, pp. 43–75, 1996.
- [5] H. Jiang, G. Larsson, M. M. G. Shakhnarovich, and E. Learned-Miller, "Self-supervised relative depth learning for urban scene understanding," in *Proceedings of the european conference on computer vision (eccv)*, 2018, pp. 19–35.
- [6] R. Blake and H. Wilson, "Binocular vision," *Vision research*, vol. 51, no. 7, pp. 754–770, 2011.
- [7] S. Ingle and M. Phute, "Tesla autopilot: semi autonomous driving, an uptick for future autonomy," *International Research Journal of Engineering and Technology*, vol. 3, no. 9, pp. 369–372, 2016.
- [8] C. Godard, O. Mac Aodha, M. Firman, and G. J. Brostow, "Digging into self-supervised monocular depth estimation," in *Proceedings of the IEEE/CVF international conference on computer vision*, 2019, pp. 3828–3838.
- [9] M. Cordts, M. Omran, S. Ramos, T. Rehfeld, M. Enzweiler, R. Benenson, U. Franke, S. Roth, and B. Schiele, "The cityscapes dataset for semantic urban scene understanding," in *Proceedings of the IEEE conference on computer vision and pattern recognition*, 2016, pp. 3213–3223.
- [10] Y. Cabon, N. Murray, and M. Humenberger, "Virtual kitti 2," 2020.
- [11] G. Ros, L. Sellart, J. Materzynska, D. Vazquez, and A. M. Lopez, "The synthia dataset: A large collection of synthetic images for semantic segmentation of urban scenes," in *Proceedings of the IEEE conference on computer vision and pattern recognition*, 2016, pp. 3234–3243.
- [12] X. Huang, X. Cheng, Q. Geng, B. Cao, D. Zhou, P. Wang, Y. Lin, and R. Yang, "The apolloscope dataset for autonomous driving," in *Proceedings of the IEEE conference on computer vision and pattern recognition workshops*, 2018, pp. 954–960.
- [13] A. Dosovitskiy, G. Ros, F. Codevilla, A. Lopez, and V. Koltun, "Carla: An open urban driving simulator," in *Conference on robot learning*. PMLR, 2017, pp. 1–16.
- [14] J. K. Haas, "A history of the unity game engine," *Diss. Worcester Polytechnic Institute*, vol. 483, no. 2014, p. 484, 2014.
- [15] A. Sanders, *An introduction to Unreal engine 4*. CRC Press, 2016.
- [16] A. Gurram, A. F. Tuna, F. Shen, O. Urfalioglu, and A. M. López, "Monocular depth estimation through virtual-world supervision and real-world sfm self-supervision," *IEEE Transactions on Intelligent Transportation Systems*, vol. 23, no. 8, pp. 12738–12751, 2021.
- [17] A. Geiger, P. Lenz, and R. Urtasun, "Are we ready for autonomous driving? the kitti vision benchmark suite," in *2012 IEEE conference on computer vision and pattern recognition*. IEEE, 2012, pp. 3354–3361.
- [18] S. Yun, D. Han, S. J. Oh, S. Chun, J. Choe, and Y. Yoo, "Cutmix: Regularization strategy to train strong classifiers with localizable features," in *Proceedings of the IEEE/CVF international conference on computer vision*, 2019, pp. 6023–6032.
- [19] M.-H. Guo, C.-Z. Lu, Z.-N. Liu, M.-M. Cheng, and S.-M. Hu, "Visual attention network," *Computational Visual Media*, vol. 9, no. 4, pp. 733–752, 2023.
- [20] Y. ZHU, R. Ren, X. Li, G. Shi *et al.*, "Tsudepth: Exploring temporal symmetry-based uncertainty for unsupervised monocular depth estimation," *Available at SSRN: https://ssrn.com/abstract=4733703 or http://dx.doi.org/10.2139/ssrn.4733703*, 2024.
- [21] C. Godard, O. Mac Aodha, and G. J. Brostow, "Unsupervised monocular depth estimation with left-right consistency," in *Proceedings of the IEEE conference on computer vision and pattern recognition*, 2017, pp. 270–279.
- [22] T. Zhou, M. Brown, N. Snavely, and D. G. Lowe, "Unsupervised learning of depth and ego-motion from video," in *Proceedings of the IEEE conference on computer vision and pattern recognition*, 2017, pp. 1851–1858.
- [23] V. Guizilini, R. Ambrus, S. Pillai, A. Raventos, and A. Gaidon, "3d packing for self-supervised monocular depth estimation," in *Proceedings of the IEEE/CVF conference on computer vision and pattern recognition*, 2020, pp. 2485–2494.
- [24] J. Yan, H. Zhao, P. Bu, and Y. Jin, "Channel-wise attention-based network for self-supervised monocular depth estimation," in *2021 International Conference on 3D Vision (3DV)*. IEEE, 2021, pp. 464–473.
- [25] X. Lyu, L. Liu, M. Wang, X. Kong, L. Liu, Y. Liu, X. Chen, and Y. Yuan, "Hr-depth: High resolution self-supervised monocular depth estimation," in *Proceedings of the AAAI Conference on Artificial Intelligence*, vol. 35, no. 3, 2021, pp. 2294–2301.
- [26] H. Zhou, D. Greenwood, and S. Taylor, "Self-supervised monocular depth estimation with internal feature fusion," *arXiv preprint arXiv:2110.09482*, 2021.
- [27] M. He, L. Hui, Y. Bian, J. Ren, J. Xie, and J. Yang, "Ra-depth: Resolution adaptive self-supervised monocular depth estimation," in *European Conference on Computer Vision*. Springer, 2022, pp. 565–581.
- [28] A. Vaswani, N. Shazeer, N. Parmar, J. Uszkoreit, L. Jones, A. N. Gomez, Ł. Kaiser, and I. Polosukhin, "Attention is all you need," *Advances in neural information processing systems*, vol. 30, 2017.
- [29] A. Dosovitskiy, L. Beyer, A. Kolesnikov, D. Weissenborn, X. Zhai, T. Unterthiner, M. Dehghani, M. Minderer, G. Heigold, S. Gelly *et al.*, "An image is worth 16x16 words: Transformers for image recognition at scale," *arXiv preprint arXiv:2010.11929*, 2020.
- [30] Z. Liu, Y. Lin, Y. Cao, H. Hu, Y. Wei, Z. Zhang, S. Lin, and B. Guo, "Swin transformer: Hierarchical vision transformer using shifted windows," in *Proceedings of the IEEE/CVF international conference on computer vision*, 2021, pp. 10012–10022.
- [31] R. Ranftl, A. Bochkovskiy, and V. Koltun, "Vision transformers for dense prediction," in *Proceedings of the IEEE/CVF international conference on computer vision*, 2021, pp. 12179–12188.
- [32] A. Varma, H. Chawla, B. Zonooz, and E. Arani, "Transformers in self-supervised monocular depth estimation with unknown camera intrinsics," *arXiv preprint arXiv:2202.03131*, 2022.
- [33] C. Zhao, Y. Zhang, M. Poggi, F. Tosi, X. Guo, Z. Zhu, G. Huang, Y. Tang, and S. Mattoccia, "Monovit: Self-supervised monocular depth estimation with a vision transformer," in *2022 International Conference on 3D Vision (3DV)*. IEEE, 2022, pp. 668–678.
- [34] N. Zhang, F. Nex, G. Vosselman, and N. Kerle, "Lite-mono: A lightweight cnn and transformer architecture for self-supervised monocular depth estimation," in *Proceedings of the IEEE/CVF Conference on Computer Vision and Pattern Recognition*, 2023, pp. 18537–18546.
- [35] Y. Lee, J. Kim, J. Willette, and S. J. Hwang, "Mpvit: Multi-path vision transformer for dense prediction," in *Proceedings of the IEEE/CVF Conference on Computer Vision and Pattern Recognition*, 2022, pp. 7287–7296.
- [36] K. Swami, A. Muduli, U. Gurram, and P. Bajpai, "Do what you can, with what you have: Scale-aware and high quality monocular depth estimation without real world labels," in *Proceedings of the IEEE/CVF Conference on Computer Vision and Pattern Recognition*, 2022, pp. 988–997.
- [37] Y. Ganin and V. Lempitsky, "Unsupervised domain adaptation by back-propagation," in *International conference on machine learning*. PMLR, 2015, pp. 1180–1189.
- [38] Y. Zhao, S. Kong, D. Shin, and C. Fowlkes, "Domain decluttering: Simplifying images to mitigate synthetic-real domain shift and improve depth estimation," in *Proceedings of the IEEE/CVF Conference on Computer Vision and Pattern Recognition*, 2020, pp. 3330–3340.
- [39] P. Isola, J.-Y. Zhu, T. Zhou, and A. A. Efros, "Image-to-image translation with conditional adversarial networks," in *Proceedings of the IEEE conference on computer vision and pattern recognition*, 2017, pp. 1125–1134.

- [40] A. Atapour-Abarghouei and T. P. Breckon, "Real-time monocular depth estimation using synthetic data with domain adaptation via image style transfer," in *Proceedings of the IEEE conference on computer vision and pattern recognition*, 2018, pp. 2800–2810.
- [41] S.-W. Huang, C.-T. Lin, S.-P. Chen, Y.-Y. Wu, P.-H. Hsu, and S.-H. Lai, "Auggan: Cross domain adaptation with gan-based data augmentation," in *Proceedings of the European Conference on Computer Vision (ECCV)*, 2018, pp. 718–731.
- [42] J. L. Gómez, G. Villalonga, and A. M. López, "Co-training for unsupervised domain adaptation of semantic segmentation models," *Sensors*, vol. 23, no. 2, p. 621, 2023.
- [43] C. Zheng, T.-J. Cham, and J. Cai, "T2net: Synthetic-to-realistic translation for solving single-image depth estimation tasks," in *Proceedings of the European conference on computer vision (ECCV)*, 2018, pp. 767–783.
- [44] T. v. Dijk and G. d. Croon, "How do neural networks see depth in single images?" in *Proceedings of the IEEE/CVF International Conference on Computer Vision*, 2019, pp. 2183–2191.
- [45] T. Sun, M. Segu, J. Postels, Y. Wang, L. Van Gool, B. Schiele, F. Tombari, and F. Yu, "SHIFT: a synthetic driving dataset for continuous multi-task domain adaptation," in *Proceedings of the IEEE/CVF Conference on Computer Vision and Pattern Recognition (CVPR)*, June 2022, pp. 21 371–21 382.
- [46] J. L. Gómez, M. Silva, A. Seoane, A. Borrás, M. Noriega, G. Ros, J. A. Iglesias-Guitián, and A. M. López, "All for one, and one for all: Urbansyn dataset, the third musketeer of synthetic driving scenes," 2023.
- [47] D. Eigen, C. Puhrsch, and R. Fergus, "Depth map prediction from a single image using a multi-scale deep network," *Advances in neural information processing systems*, vol. 27, 2014.
- [48] R. Gao, "Rethinking dilated convolution for real-time semantic segmentation," in *Proceedings of the IEEE/CVF Conference on Computer Vision and Pattern Recognition*, 2023, pp. 4674–4683.
- [49] K. He, X. Zhang, S. Ren, and J. Sun, "Deep residual learning for image recognition," in *Proceedings of the IEEE conference on computer vision and pattern recognition*, 2016, pp. 770–778.
- [50] K. Sun, B. Xiao, D. Liu, and J. Wang, "Deep high-resolution representation learning for human pose estimation," in *Proceedings of the IEEE/CVF conference on computer vision and pattern recognition*, 2019, pp. 5693–5703.
- [51] T.-W. Hui, "Rm-depth: Unsupervised learning of recurrent monocular depth in dynamic scenes," in *Proceedings of the IEEE/CVF Conference on Computer Vision and Pattern Recognition*, 2022, pp. 1675–1684.
- [52] Y. Zhu, W. Dong, L. Li, J. Wu, X. Li, and G. Shi, "Robust depth completion with uncertainty-driven loss functions," in *Proceedings of the AAAI Conference on Artificial Intelligence*, vol. 36, no. 3, 2022, pp. 3626–3634.
- [53] R. Ranftl, K. Lasinger, D. Hafner, K. Schindler, and V. Koltun, "Towards robust monocular depth estimation: Mixing datasets for zero-shot cross-dataset transfer," *IEEE transactions on pattern analysis and machine intelligence*, vol. 44, no. 3, pp. 1623–1637, 2020.
- [54] L. Yang, B. Kang, Z. Huang, X. Xu, J. Feng, and H. Zhao, "Depth anything: Unleashing the power of large-scale unlabeled data," *arXiv preprint arXiv:2401.10891*, 2024.
- [55] A. Paszke, S. Gross, F. Massa, A. Lerer, J. Bradbury, G. Chanan, T. Killeen, Z. Lin, N. Gimelshein, L. Antiga *et al.*, "Pytorch: An imperative style, high-performance deep learning library," *Advances in neural information processing systems*, vol. 32, 2019.
- [56] D. P. Kingma and J. Ba, "Adam: A method for stochastic optimization," *arXiv preprint arXiv:1412.6980*, 2014.
- [57] V. Casser, S. Pirk, R. Mahjourian, and A. Angelova, "Depth prediction without the sensors: Leveraging structure for unsupervised learning from monocular videos," in *Proceedings of the AAAI conference on artificial intelligence*, vol. 33, no. 01, 2019, pp. 8001–8008.
- [58] Y. Chen, C. Schmid, and C. Sminchisescu, "Self-supervised learning with geometric constraints in monocular video: Connecting flow, depth, and camera," in *Proceedings of the IEEE/CVF International Conference on Computer Vision*, 2019, pp. 7063–7072.
- [59] A. Gordon, H. Li, R. Jonschkowski, and A. Angelova, "Depth from videos in the wild: Unsupervised monocular depth learning from unknown cameras," in *Proceedings of the IEEE/CVF International Conference on Computer Vision*, 2019, pp. 8977–8986.
- [60] H. Li, A. Gordon, H. Zhao, V. Casser, and A. Angelova, "Unsupervised monocular depth learning in dynamic scenes," in *Conference on Robot Learning*. PMLR, 2021, pp. 1908–1917.
- [61] S. Lee, S. Im, S. Lin, and I. S. Kweon, "Learning monocular depth in dynamic scenes via instance-aware projection consistency," in *Proceedings of the AAAI Conference on Artificial Intelligence*, vol. 35, no. 3, 2021, pp. 1863–1872.
- [62] J. Bae, S. Moon, and S. Im, "Deep digging into the generalization of self-supervised monocular depth estimation," in *Proceedings of the AAAI conference on artificial intelligence*, vol. 37, no. 1, 2023, pp. 187–196.
- [63] M. Klingner, J.-A. Termöhlen, J. Mikolajczyk, and T. Fingscheidt, "Self-supervised monocular depth estimation: Solving the dynamic object problem by semantic guidance," in *Computer Vision—ECCV 2020: 16th European Conference, Glasgow, UK, August 23–28, 2020, Proceedings, Part XX 16*. Springer, 2020, pp. 582–600.
- [64] R. Wang, Z. Yu, and S. Gao, "Planedepth: Self-supervised depth estimation via orthogonal planes," in *Proceedings of the IEEE/CVF Conference on Computer Vision and Pattern Recognition*, 2023, pp. 21 425–21 434.